pH-responsive hollow core zeolitic-imidazolate framework-8 as an effective drug carrier of 5-fluorouracil

S.A. Anggraini [a, f], K.A. Prasetija [a, f], M. Yuliana [a, *], C.J. Wijaya [a, **], V. Bundjaja [b], A.E. Angkawijaya [c, d], Y.-F. Jiang [e], J.N. Putro [a], S.B. Hartono [a], A. Ayucitra [a], S.P. Santoso [a, b], S. Ismadji [a, b], F.E. Soetaredjo [a, b]

[a] Department of Chemical Engineering, Widya Mandala Surabaya Catholic University, Kalijudan 37, Surabaya 60114, Indonesia
[b] Department of Chemical Engineering, National Taiwan University of Science and Technology, 43, Keelung Rd., Sec.4, Taipei 10607, Taiwan
[c] Graduate Institute of Applied Science and Technology, National Taiwan University of Science and Technology, 43 Keelung Road, Sec 4, Taipei, 10607, Taiwan
[d] Plant Lipid Research Team, RIKEN Center for Sustainable Resource Science, Yokohama 230-0045, Japan
[e] Graduate Institute of Molecular and Comparative Pathobiology, School of Veterinary Medicine, National Taiwan University, Taipei, Taiwan

ARTICLE INFO

ABSTRACT

To enhance the porosity and accessibility, a novel drug carrier, the hollow core zeolitic-imidazolate framework-8 (HZIF-8), is designed using polystyrene as a hard template to sequentially load and release 5-fluorouracil (FU). HZIF-8 is signified by a large surface area and pore volume, reaching 1727.1 m^2/g and 0.99 cm^3/g, respectively. The obtained HZIF-8 exhibits rhombic dodecahedron morphology with a uniform particle size of 450 nm. The integrated hollow core is observed at *ca.* 180 nm. Evaluation of the FU encapsulation behavior in HZIF-8 nanospheres is demonstrated via the adsorption kinetics, isotherm, and thermodynamic studies. The maximum FU uptake is monitored at 40 °C with the loading capacity of 161.9 mg/g. This study suggests that the FU uptake follows the pseudo-second-order law and multilayer mechanism. The governing mechanism is chemical binding in its first layer and physical interaction in the upper layers. The release study of FU from FU-loaded HZIF-8 shows that the cumulative release at pH 5.5 (92.03%) is four times higher than that at pH 7.4 (23.31%), indicating a stimulus-responsive release mechanism where pH is required as an internal stimulus factor.

1. Introduction

5-Fluorouracil (FU) is classified as a cytotoxic drug and is mainly used for the treatment of breast, head and neck, colorectal, stomach, skin, and pancreatic cancers [1]. This drug is commonly applied intravenously and works by interfering with the growth of DNA and RNA in the cancer cells, causing incomplete cell growth and preventing these cells from proliferating [2]. During the application, most cancer drugs, including FU, require a suitable drug delivery system (DDS) to effectively treat the tumors. DDS can be employed by loading the drug into a nano-sized carrier, where this carrier helps to (1) control the release of the drug into the systemic circulation and tumor sites, (2) improve the selectivity, effectiveness, and safety of the drug administration [3,4]. For a successful DDS,

two critical aspects must be owned by the drug carrier, i.e. pore accessibility and responsiveness to pH.

Porous metal-organic frameworks (MOFs) are the new class of nanoporous materials consisting of multiple metal ions and polyfunctional organic ligands [5]. They have been widely employed in many applications, namely drug delivery, gas storage, separation, and catalysis [6,7], due to their ultra-high surface area and pore volume [8,9], low densities, well-defined pores [10,11], tunable functionalities, diverse structures [12,13], high stability [14], tenability in various conditions, and facile modification [15]. MOFs also possess excellent biodegradability and low cytotoxicity, which rendered this material the ideal candidate for hosting drug materials [16,17]. However, to date, significant progress has been made mainly in the design and fabrication of nanoscale and microporous MOFs [18−20]. While MOFs generally have adequate pore size (up to 6 nm) to load most small-molecule cancer drugs, including FU, many studies strive to increase the drug intake into the carrier and reduce the intensity of the drug administration, which is important to lower down the side-effects and resulting complications [21].

* Corresponding author.
** Corresponding author.
E-mail addresses: mariayuliana@ukwms.ac.id (M. Yuliana), ch.julius7@gmail.com (C.J. Wijaya).
[f] These authors contributed equally to this work.

As pore accessibility of the drug carriers is classified as the governing factor for a successful DDS, MOFs with integrated pores certainly provide a higher accessibility for the drug molecules to diffuse in and out from the materials [18]. Few approaches have been conducted to prepare this type of MOF; one of them is to utilize polymer nanoparticles as a hard template to create a rattle-like core inside MOFs. The removal of the hard template through core etching using dimethylformamide (DMF) produces an integrated pore framework (hollow core) inside MOFs [12] and opens additional surface area that is highly accessible. This modification is expected to increase the drug's effectiveness and accessibility.

Of several available MOF structures, zeolitic-imidazolate framework-8 (ZIF-8) is selected due to its (1) exceptional chemical and thermal stability [3,22,23], (2) sodalite topology which is easy for the fabrication of hollow structure [12], (3) modifiable pore volume and surface area [24,25], and (4) sensitivity to pH. Kaur et al. (2017) studied that the mercaptopurine drug loaded into ZIF-8 nanoparticles had a release time of 10 h and seven days, respectively, at a pH of 5.5 and 7.4 [3]. This shows that ZIF-8 forms a closed conformation at physiological pH (pH = 7.4) and opens its confinement at lower pH values. As the pH of the cancerous extracellular environment is at 5−6, we consider ZIF-8, in particular hollow ZIF-8 (HZIF-8), as a suitable carrier for cancer drugs. In this study, polystyrene (PS) is used as the hard template to ensure the formation of hollow-core structure and the uniformity of particle size.

In the present study, we investigate the potential application of HZIF-8 to increase the loading capacity and accessibility of FU and promote the release of FU. The loading behavior of FU into HZIF-8 is evaluated at various temperatures (T, K), and the loaded mass of HZIF-8 (m_c, g), and elucidated using the kinetic, isotherm, and thermodynamic studies. The FU release profile is also implemented and studied at pH 5.5 and 7.4 to prove its responsiveness to pH.

2. Materials and methods

2.1. Materials

Potassium persulfate ($K_2S_2O_8$, CAS No. 7727-21-1, ≥99.0% purity), styrene ($C_6H_5CHCH_2$, CAS No. 100-42-5, ≥99.0% purity), methacrylic acid ($C_4H_6O_2$, CAS No. 79-41-4, ≥99.0% purity), zinc nitrate hexahydrate ($Zn(NO_3)_2 \cdot 6H_2O$, CAS No. 10196-18-6, ≥99.0% purity), 2-methylimidazole (Hmim, $C_4H_6N_2$, CAS No. 693-98-1, 99.0% purity), DMF ($HCON(CH_3)_2$, CAS No. 68-12-2, ≥99.8% purity), methanol (CH_3OH, CAS No. 67-56-1, ≥99.8% purity), 5-FU ($C_4H_3FN_2O_2$, CAS No. 51-21-8, ≥99.0% purity), phosphate buffer saline (PBS), hydrochloric acid (HCl, CAS No. 7647-01-0, ≥37.0% purity), and sodium hydroxide (NaOH, CAS No. 1310-73-2, ≥97.0% purity) are purchased from Sigma Aldrich (Germany) in analytical grade and used without further purification.

2.2. Preparation of PS template

Potassium persulfate solution is prepared by dissolving 0.2 g $K_2S_2O_8$ in 160 mL deionized water under continuous stirring at 300 rpm. Sequentially, styrene (18 mL), and methacrylic acid (2 mL) are added to the solution. The mixture is then continuously stirred at 80 °C for 24 h before being freeze-dried at −42 °C and 40 mbar to obtain the PS solid which is used as the template to fabricate the hollow core of HZIF-8.

2.3. Synthesis of HZIF-8

HZIF-8 is synthesized through three growth cycles of ZIF-8 on the PS template. For the first growth cycle, three solutions are individually prepared, e.g. (A) 0.5 g PS dispersed in 15 mL methanol, (B) zinc nitrate solution in methanol (2.5% w/v, 40 mL), and (C) Hmim solution in methanol (5.5% w/v, 40 mL). Initially, solution B is added to the PS suspension (A) and stirred at 300 rpm for 10 min. Then, solution C is added dropwise to the mixture; the precipitation occurs in this step. The mixture is continuously stirred at room temperature for 4 h and followed by 10-min heating at 60 °C. The PS@ZIF-8 solids are collected by centrifugation at 6000 rpm for 5 min, washed twice with methanol, and oven-dried at 60 °C. The second and third growth cycles are carried out using the same procedures to provide a robust HZIF-8 shell structure. To remove the PS template, the dried PS@ZIF-8 solids are immersed in 50 mL DMF for 6 h at room temperature under continuous stirring. The remaining solids are separated from the supernatant by centrifugation, washed twice with methanol, and dried at 60 °C to obtain HZIF-8 particles.

2.4. Characterizations

HZIF-8 is characterized by scanning electron microscopy-energy dispersive X-Ray spectroscopy (SEM-EDX), transmission electron microscopy (TEM), X-ray powder diffraction (XRD), and nitrogen (N_2) sorption. The SEM-EDX images are acquired using a JEOL JSM-6500 F (Jeol Ltd., Japan) at an accelerating voltage of 15 kV and a working distance of 10.6 mm, while the TEM analysis is conducted using JEOL JEM-2100 (Jeol Ltd., Japan) at 200 kV. The crystal structure of HZIF-8 is presented by XRD analysis within the 2θ range of 5−50° using an X'PERT Panalytical Pro X-ray diffractometer (Philips-FEI, Netherlands) with Cu K$_{\alpha 1}$ radiation (λ = 1.5406 Å) at 40 kV and 30 mA. The N_2 sorption analysis is performed to measure the textural properties of HZIF-8, e.g. specific surface area (S_{BET}), pore volume (V_p), and mean pore diameter (d_p). This analysis is carried out at 77 K using a Micromeritics ASAP 2010 sorption analyzer (Micromeritics Instrument Corporation, USA) after degassing the sample for 2 h at 423 K. The point of zero charge (pH_{pzc}) of HZIF-8 is measured using the drift method at pH = 2−10.

2.5. Adsorption kinetics and isotherm of FU onto HZIF-8

All adsorption experiments are carried out using a 5-mL FU solution (500 mg/L) for each adsorption batch at neutral pH. The kinetic study is performed by adding 50 μg HZIF-8 to a series of adsorption batches, and each batch is collected at different time intervals, ranging from $t = 10$ min to $t = 24$ h, to measure the loaded amount of FU in HZIF-8 and find the equilibrium time (t_{eq}). Meanwhile, the isotherm study uses various initial FU concentrations (25−500 ppm) with the HZIF-8 loading and adsorption time of 50 μg and t_{eq}, respectively. The concentration of the remaining FU in the supernatant is measured using Shimadzu ultraviolet-visible (UV−Vis) spectrophotometer 2600 (Shimadzu, Japan) at a wavelength (λ) of 265.5 nm. This specific wavelength is obtained from the analysis of UV−Vis spectrum profile of a standard FU solution at λ = 190−900 nm, and refers to the wavelength where FU has its strongest photon absorption. Three levels of temperature (30, 40, and 50 °C) are employed to study its influence on drug uptake.

The adsorption capacities at a certain time (q_t, mg/g) and at equilibrium (q_e, mg/g) are calculated using the following equations.

$$q_t = \frac{(C_0 - C_t)V}{m_c} \tag{1}$$

$$q_e = \frac{(C_0 - C_e)V}{m_c} \tag{2}$$

where the terms of C_0, C_t, and C_e (mg/L) correspond to the initial FU concentration, the remaining FU concentration at a certain time t, and the remaining FU concentration at the equilibrium stage in the solution, respectively. Meanwhile, V (L) and m_c (g) are, respectively, defined as the volume of FU solution and the amount of HZIF-8. The kinetics and isotherm data are then fitted with several adsorption models to evaluate the adsorption mechanism. Moreover, the obtained isotherm parameters are used to investigate the adsorption thermodynamics properties, including the Gibbs free energy ($\Delta G°$), enthalpy ($\Delta H°$), and entropy ($\Delta S°$).

2.6. Release study of FU from FU-loaded HZIF-8

The release of FU from the FU-loaded HZIF-8 (FU@HZIF-8) is performed by introducing 200 mg of FU@HZIF-8 into a 5 mL PBS solution (as the release medium) in the dialysis membrane. The dialysis membrane containing the mixture above is then immersed in 500 mL PBS solution at 37 °C under slow constant stirring. Five-milliliters solution is withdrawn at various release duration, with the range of 10 min−4 days, and subsequently analyzed using Shimadzu UV−Vis spectrophotometer 2600 (Shimadzu, Japan) at a wavelength (λ) of 265.5 nm. At the same time, the solution taken during sampling is replaced with a fresh PBS solution to maintain the total release volume. The release system is adjusted to pH = 5.5 and pH = 7.4 using 2 N HCl and 1 N NaOH solutions to simulate the blood plasma condition and to monitor the responsiveness of HZIF-8 at various pHs.

3. Results and discussion

3.1. Characterization of HZIF-8

Fig. 1a shows the spherical morphology of the PS template, while the SEM and TEM images of HZIF-8 are presented in Figs. 1b−c. The PS template has a uniform particle diameter, ranging from 190 to 200 nm. Meanwhile, HZIF-8 reveals its rhombic dodecahedron structure with a uniform particle diameter at *ca.* 450 nm. This morphology is consistent with the previous studies that use similar solvent and metal to ligand molar ratios [26−28]. Notably, the TEM image (Fig. 1c), along with Fig. 1b (inset), confirms the hollow structure of HZIF-8 with the size of 180 nm. The shell of HZIF-8 is estimated at *ca.* 135 nm and contains the framework of zinc as the metal node and Hmim as the ligand linker. The open hollow core, seen in Fig. 1b (inset), might be caused by the template removal process. The offered interior structure of HZIF-8 has the potential to be used as a drug carrier, as it provides high accessibility for drugs to enter and attach to its surface.

The elemental composition of HZIF-8, obtained from the EDX analysis (Fig. 1d), demonstrates the presence of zinc, carbon, oxygen, and nitrogen with the atomic composition of 7.76%, 46.50%, 7.35%, and 38.39%, respectively. This result proves that HZIF-8 is composed of the elements from its precursors. Binaeian et al. (2020) reported a similar atomic composition of ZIF-8 [29], implying that there is no elemental change during the integration of the hollow core to ZIF-8. The elemental mapping of HZIF-8 (Figs. 1e−h) also exhibits the uniform distribution of zinc, carbon, oxygen, and nitrogen in the material.

The XRD spectra of HZIF-8 and ZIF-8 are presented in Fig. 2a. Strong crystal peaks at $2\theta = 7.42°$ (011), 10.45° (002), 12.77° (112), 14.79° (022), 16.50° (013), and 18.12° (222) are observed for both materials, which agrees with those reported by Beh et al. (2017) [27]. With the similar diffraction profiles, it can be concluded that there is no change in the crystal configuration of ZIF-8 and HZIF-8. The textural properties of HZIF-8, including S_{BET}, V_p, d_p, are obtained using N$_2$ sorption analysis at 1727.1 m^2/g, 0.99 cm^3/g,

and 2.30 nm, respectively. These results demonstrate that HZIF-8 indeed has a larger accessibility than the common ZIF-8 (S_{BET} = 1384.1 m^2/g, V_p = 0.65 cm^3/g, and d_p = 1.87 nm). This structure modification has been successfully developed to create HZIF-8 with better physical properties and greater potential for enhancing the adsorption ability. The N$_2$ adsorption/desorption profiles (Fig. 2b) of both materials exhibit the type-I isotherm [30], with the hysteresis model of H4, implying the presence of slit-shaped pores in the mesoporous size range [31]. The over-lapping adsorption and desorption curves point to the reversible sorption process and the independence of adsorption and desorption systems [32,33]. This proves that HZIF-8 has high accessibility which is good for a drug carrier material. The pH$_{pzc}$ of HZIF-8 is obtained at pH = 9.1, which shares a similar value to the pH$_{pzc}$ of ZIF-8 at 9.3, indicating that integrating the hollow core to the ZIF-8 does not change the chemical properties of the material. This result also implies that HZIF-8 has a positive charge (cationic) at pH lower than pH$_{pzc}$ and is negatively charged at pH > pH$_{pzc}$.

3.2. The kinetic study of FU uptake onto HZIF-8

This study employs two empirical kinetic models, pseudo-first-order (PFO) and pseudo-second-order (PSO), to fit the adsorption data. Fig. 3 shows that the uptake of FU onto HZIF-8 increases significantly from the initial condition to the first 10 min, and gradually rises its capacity until it reaches the equilibrium at 3 h. The vertically inclined curve observed in the early stage of adsorption indicates the occurrence of burst adsorption during the bulk diffusion stage, where the FU molecules are transferred from the solution to a liquid film on the surface of HZIF-8. The curved line from $t = 1$ h to $t = 3$ h denotes the film migratory of FU passing through the boundary layer of HZIF-8. The third step, indicated by the plateau area, implies the equilibrium condition of the FU uptake, where FU diffuses within the HZIF-8 particle into its interior part [34].

According to the parameters obtained from the non-linear fitting of PFO and PSO models (Table 1), the R^2 value of the PSO model is higher than that of the PFO model, which means that the FU uptake on HZIF-8 is better expressed through the PSO model. Based on the kinetic profiles, the equilibrium time is obtained at 3 h, while the highest uptake capacity of FU is monitored at 40 °C with the value of 161.9 mg/g. The k_1 constants of the PFO model at all tested temperatures give very high values, which indicate extremely fast adsorption to reach the equilibrium. This is no less consistent with experimental data which showed that the equilibrium stage is reached at 3 h adsorption time. Meanwhile, the k_2 values of the PSO model are inversely proportional to the increase in temperature. This trend is mainly attributed to the tendency of the FU molecules to detach from the surface of HZIF-8 due to the increasing collision intensity between FU and HZIF-8 at higher temperatures [35,36]. However, an increase in temperature will also trigger the accelerated kinetic motion of the adsorbate in the bulk solution, which promotes the energy barrier to be exceeded and encourages the rate of intraparticle diffusion [36]. This phenomenon is indicated by the escalation of Q_e values from 30 °C to 40 °C presented in Table 1. The rising value of Q_e along with temperature exhibiting the endothermic process can be also affected by the pore size enlargement, surface activation, or the emergence of new active sites [37]. Meanwhile, the Q_e value is observed to be lower at 50 °C, which might be caused by the aggregation of adsorbents in the adsorption system which blocks the active sites of the adsorbent [38].

The better fitted PSO model implies the fact that the rate-limiting step in this FU uptake is inclined to chemisorption, with
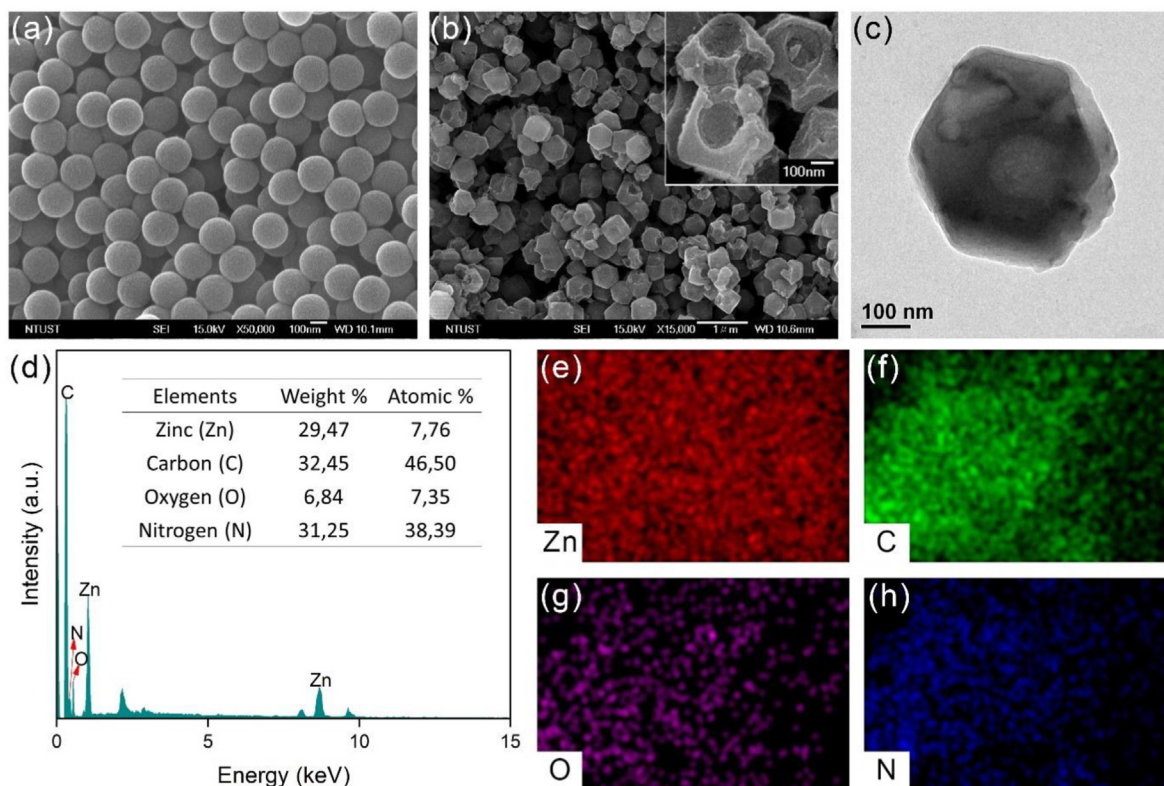
Fig. 1. SEM images of (a) PS and (b) HZIF-8, (c) TEM image of HZIF-8, (d) EDX of HZIF-8, and (e−h) the elemental mapping of HZIF-8. EDX, energy-dispersive X-ray spectroscopy; HZIF, hollow zeolitic-imidazolate framework; SEM, scanning electron microscopy.
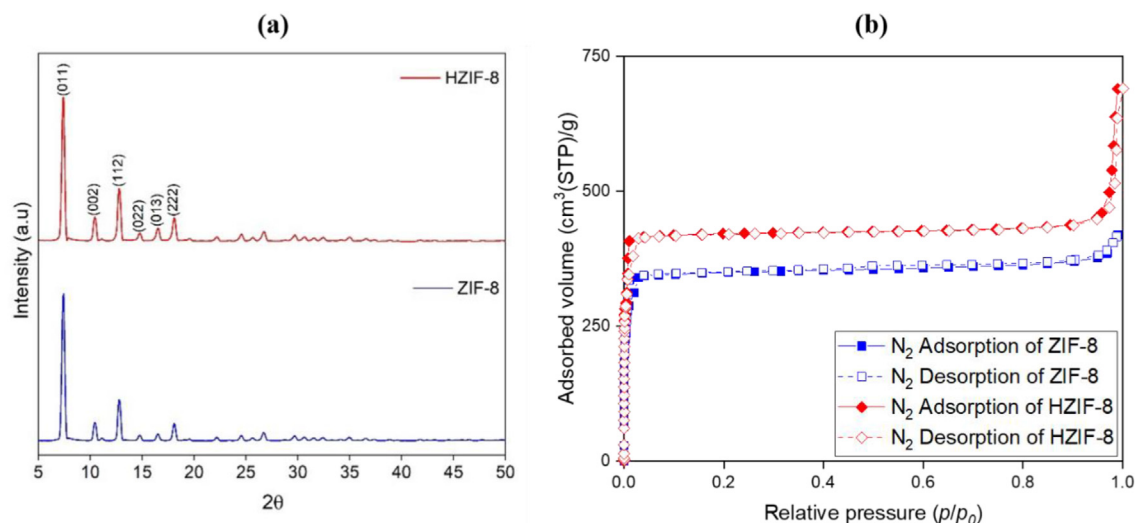

Fig. 2. (a) The XRD analysis and (b) N_2 adsorption/desorption profile of HZIF-8 and ZIF-8. HZIF, hollow zeolitic-imidazolate framework; XRD, X-ray powder diffraction; ZIF, zeolitic-imidazolate framework.

the involvement of the electron transfer or exchange between HZIF-8 and FU [39]. The driving force of this migration is predicted to be the rapid exchange of ions from the surface functional groups on the adsorbent followed by a diffusion process [40,41]. This result is also supported by the pH$_{pzc}$ study, where during the adsorption at pH = 7 (pH < pH$_{pzc}$), the HZIF-8 particles are present in a cationic form, and associate with the anionic FU via the electrostatic interaction. Moreover, HZIF-8 provides abundant active sites, which underlie the possible π-interaction and hydrogen bonding

mechanism between FU and HZIF-8. The π-interaction occurs because ZIF-8, as the basic framework of HZIF-8, has two double bonds and a pair of electrons from nitrogen which are very useful for interacting with FU via hydrogen bonding [42]. To improve the understanding of the interactions between HZIF-8 and FU, the possible binding mechanism is illustrated in Fig. 4. Additionally, the adsorption capacities of ZIF-8 and HZIF-8 are also compared at the same operating condition, where the adsorption capacity of HZIF-8 is found at 140.1 mg/g, almost 2-folds higher than that of ZIF-8. This
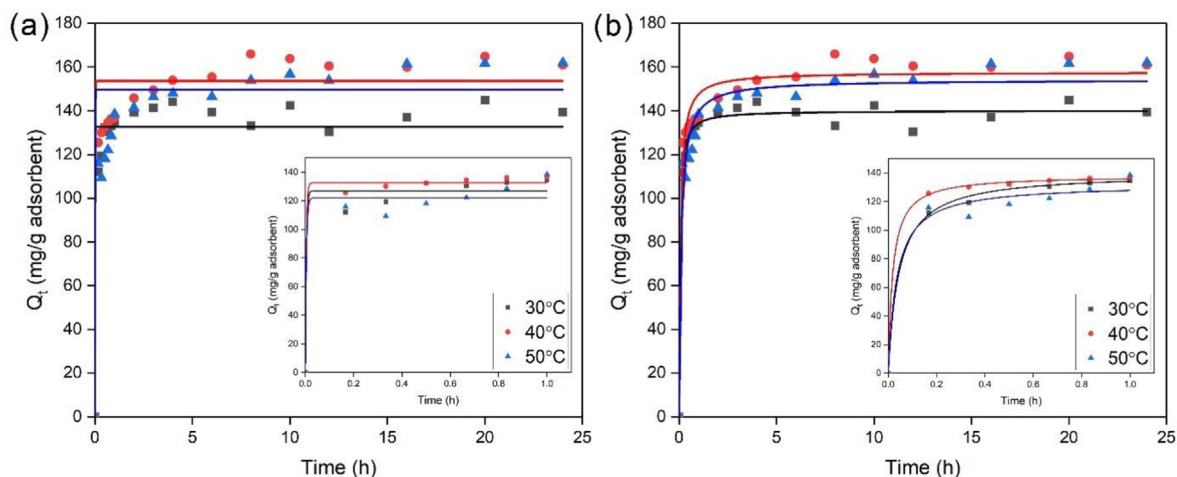
Fig. 3. The kinetic data of FU uptake on HZIF-8, fitted using (a) pseudo-first order and (b) pseudo-second order models. FU, fluorouracil; HZIF, hollow zeolitic-imidazolate framework.

Table 1
The computed kinetic parameters of the FU uptake onto HZIF-8.

T (°C)	Q_{exp} (mg/g)	PFO model			PSO model		
		k_1 (1/min)	Q_e (mg/g)	R^2	k_2 (g/mg.min)	Q_e (mg/g)	R^2
30	139.4	174.7	132.7	0.9286	0.164	140.1	0.9856
40	161.9	111.5	153.6	0.8491	0.092	157.7	0.9633
50	160.9	133.6	149.8	0.7403	0.061	154.2	0.9507

proves the successful development of HZIF-8 which has greater potential as a drug carrier.

3.3. Adsorption isotherm study

Fig. 5 shows the isotherm profile of the FU uptake in terms of Q_e vs. C_e; three fitting models have been used to characterize the adsorption behavior. Supported by the highest R^2 values, the Brunauer−Emmett−Teller (BET) model provides the best fit to the adsorption isotherm data compared to the Langmuir and

Freundlich (Fig. 5a, at 40 °C), and a similar trend is observed at all temperature levels (Fig. 5b). Based on the R^2 values, the Freundlich model conforms to the equilibrium adsorption data better than the Langmuir. This empirically shows that (1) the adsorbent has a heterogeneous surface and different adsorption potentials [43] and (2) a multilayer mechanism occurs in the system [44]. The fitting of the data to the Freundlich isotherm results in the n_F values lower than unity, emphasizing the heterogeneity of the HZIF-8 surface where the FU molecules will attach to the stronger binding sites [45]. This multilayer mechanism is also supported by the fact that
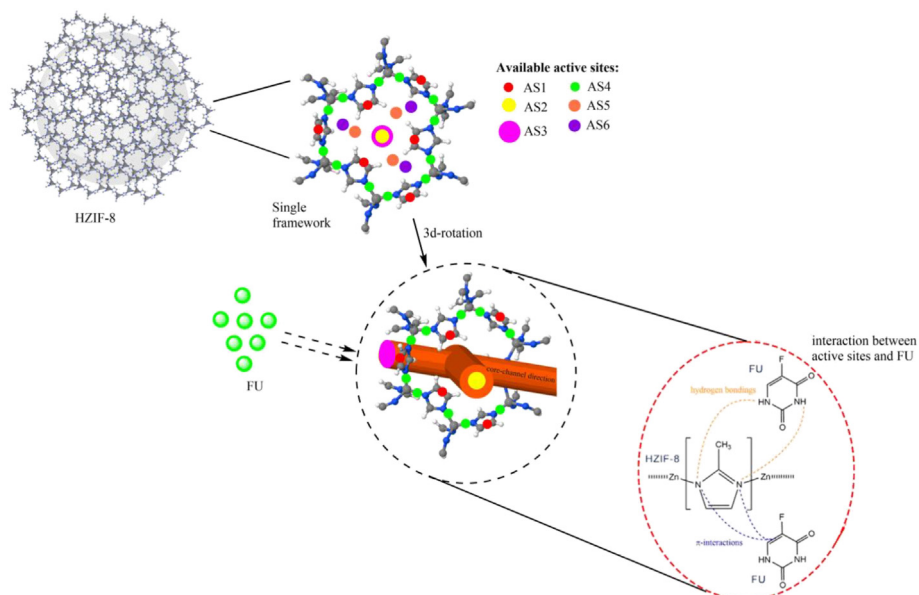

Fig. 4. Illustrations of HZIF-8 active sites and binding mechanism of FU on HZIF-8. FU, fluorouracil; HZIF, hollow zeolitic-imidazolate framework.
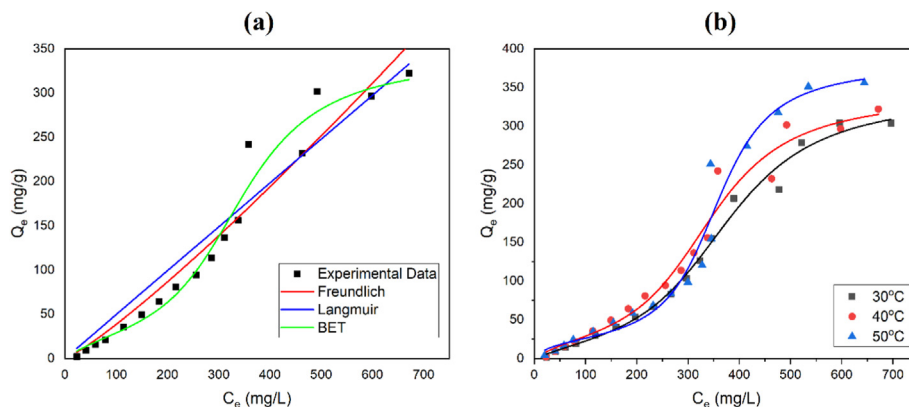
Fig. 5. The isotherm profile of the FU uptake on HZIF-8 (a) using various isotherm models at 40 °C and (b) using BET model at 30, 40, and 50 °C. BET, Braunauer–Emmett–Teller; FU, fluorouracil; HZIF, hollow zeolitic-imidazolate framework.

Table 2
The fitted isotherm parameters for the FU uptake onto HZIF-8.

Models	Parameters	T (°C)		
		30	40	50
Langmuir	K_L	5.98×10^{-7}	1.05×10^{-6}	4.56×10^{-7}
	Q_{max}	7.52×10^5	4.71×10^5	1.20×10^6
	R^2	0.9304	0.9289	0.8556
Freundlich	K_F	0.082	0.180	0.045
	n_F	0.784	0.858	0.708
	R^2	0.9590	0.9408	0.9078
BET	n_B	10.38	10.92	17.27
	K_{FL}	0.007	0.013	0.037
	K_{UL}	0.003	0.003	0.003
	$Q_{max,BET}$	33.74	32.04	22.55
	R^2	0.9887	0.9684	0.9618

the data can be depicted very well by the BET model with the number of layers presented as n_B (Table 2). Furthermore, based on Giles' classification, the S-shaped uptake profile (as seen in Fig. 5) indicates the occurrence of cooperative adsorption, where strong interaction between the adsorbed FU molecules and the new adsorbate is observed, and therefore, creates more than one layer of FU on the surface of HZIF-8 [46,47]. This S-class is denoted by the low uptake rate and low HZIF-8/FU interactions at low initial concentrations [48]. However, at high initial concentrations, this profile sees a condensation phenomenon on the surface of HZIF-8 where every active site can be occupied by a large number of FU molecules [30].

As seen in Table 2, the number of adsorption layers (n_B) enhances with the increasing temperature and is accompanied by a decrease in the uptake capacity ($Q_{max,BET}$) of the first adsorption layer. The results present that the temperature rise causes FU to be adsorbed on the upper layers and has the potential to weaken the interaction between HZIF-8 and FU, which in the cases of drug delivery, will be beneficial to facilitate the release of the adsorbate. A large number of layers also prove that HZIF-8 possesses many active sites to provide multiple physical and chemical interactions. Referring to ZIF-8 as the basic framework for HZIF-8, there are at least six main active sites in the framework (Fig. 4), e.g. Hmim site (AS1), two locations of pore channels (AS2 and AS3), face-centered site of the pores (AS4), and two other locations near the 11 Å cage sites (AS5 and AS6) [49]. AS1, AS2, and AS3 play a strong role in the FU uptake, as they are located in the outermost perimeter and have the first contact with FU. These three active sites promote π-interaction between HZIF-8 and FU. Meanwhile, the other active

sites (AS4, AS5, and AS6) provide extra beneficial roles to strengthen their physical and chemical interactions.

The adsorption mechanism on HZIF-8 can be divided into three sequential sections as shown in Fig. 5b. First, the adsorption of FU at lower initial concentration intervals (0–200 mg/L) describes the diffusion of FU to the outer surface of HZIF-8. Second, the sharply inclined curve at concentration intervals of 200–550 mg/L indicates the diffusion of FU through the hollow and pores of HZIF-8 occupying every active site on HZIF-8. The presence of hollow and pores triggers an increase in the diffusion rate of the adsorbate to the adsorbent so that the adsorption capacity becomes higher [50]. Third, the final adsorption profile at the initial FU concentration above 550 mg/L shows a horizontal plateau curve, denoting the equilibrium stage of the adsorption. At high FU concentration, a strong competition between FU molecules to bind onto HZIF-8 occurs, hence, promoting the resistance to the adsorption process.

3.4. Adsorption thermodynamic study

In this study, the thermodynamic study is established to further investigate the adsorption mechanism and thermodynamic properties. Herein, the activation energy (E_a), enthalpy change (ΔH^0), entropy change (ΔS^0), and Gibbs energy (ΔG^0) are evaluated using the equations as follows [51–53],

$$ln\ k_2 = ln\ A \times \frac{E_a}{RT} \tag{3}$$

$$\Delta G^0 = -RT \ln K \tag{4}$$

$$\ln K = \frac{\Delta S^0}{R} - \frac{\Delta H^0}{RT} \tag{5}$$

$$K = 1000 K_e M_{FU} C^0 \tag{6}$$

where k_2 (g/mg.min) is the equilibrium rate constant obtained from the PSO model, A is the Arrhenius constant, and E_a (kJ/mol) is the activation energy. In addition, K and K_e, respectively correspond to the thermodynamic equilibrium constant and the BET constant (K_{FL} or K_{UL}) as the best-fitted model. Meanwhile, M_{FU} and C^0 are the molecular weight of FU and the standard FU concentration (1 mol/L), respectively.

As seen in Fig. 6a, the linear regression provides the E_a value of 36.24 kJ/mol, which indicates that the adsorption mechanism is mainly governed by physical interaction [51]. However, the enthalpy

properties of the first and upper layers evaluated using the BET parameters (Fig. 6b and Table 3) are found to be at 66.08 and 3.08 kJ/mol, respectively. This illustrates that two different adsorption mechanisms occur in the system; the first layer of FU binds chemically onto the surface of HZIF-8 ($20.90 < \Delta H^0 < 418.40$ kJ/mol), while the upper FU layer interacts with HZIF-8 and adsorbed FU by the physical means ($2.10 < \Delta H^0 < 20.90$ kJ/mol) [53]. This verifies why the adsorption kinetics study is well-fitted to the PSO model but the magnitude of the activation energy tends to indicate the physisorption mechanism. Moreover, the positive value of ΔH^0 strengthens the finding that this adsorption process is endothermic [54]. The positive ΔS^0 values at both the first (0.274 kJ/mol.K) and upper (0.059 kJ/mol.K) layers imply the spontaneous adsorption process and the increasing randomness at the mass-transfer interface [52]. This result shows conformity to the negative ΔG^0 values in all layers and temperature levels, which exposes the same spontaneous process with high adsorbent-adsorbate affinity [37].

3.5. Drug release study

To investigate the pH-responsiveness of HZIF-8, the release study is carried out in the PBS solution at pH = 5.5 and pH = 7.4, and the profile is presented in Fig. 7. The drug release profile at pH = 7.4 signifies a sustained release of FU, where the release rate of FU is maintained to result in a constant drug concentration in the medium [55,56]. This type of release may potentially prolong the therapeutic effect of a drug in the body. Meanwhile, a slow first-order release profile is observed at pH = 5.5, where the FU release is rapid in the early stage and continued by a constant release rate to sustain the required drug supply to the target [56,57]. This slow first-order release is considered to be more favorable because the drug consumption can be well-controlled to provide a stable therapeutic effect over a longer period.

Considering the pH-responsiveness, the release of FU from FU@HZIF-8 indicates a stimulus-responsive release mechanism where pH is required as an internal stimulus factor [55]. In Fig. 7, the cumulative release at pH 5.5 is observed at 92.03%, around 4-folds higher than that at pH 7.4 (23.31%). It proves the pH-responsiveness nature of HZIF-8 [58], which is very beneficial in the anticancer drug (e.g. FU) release. The release mechanism of FU from FU@HZIF-8 in pH 5.5 can be divided into two main steps (Fig. 8): (1) initially, the PBS solution begins to enter HZIF-8 and interacts with the FU molecules on the surface of HZIF-8. The FU molecules are then desorbed and dissolved into the medium, (2)

Table 3
Thermodynamic properties of the FU uptake on HZIF-8.

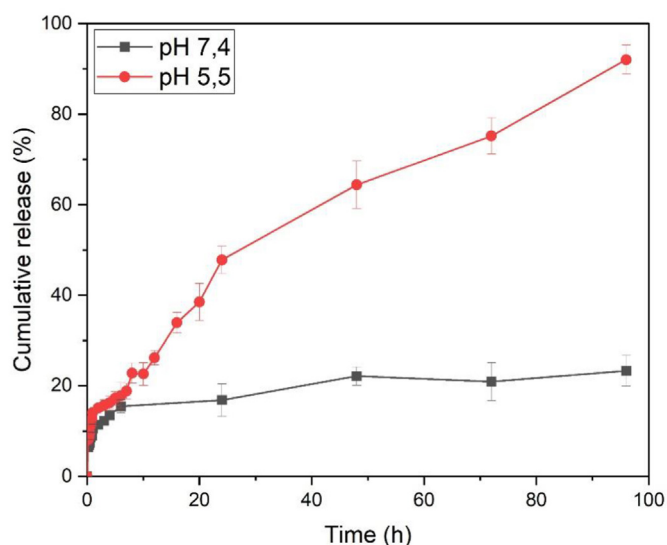| BET model	T (°C)	Properties		
		ΔH^0 (kJ/mol)	ΔS^0 (kJ/mol.K)	ΔG^0 (kJ/mol)
First layer	30	66.08	0.274	−17.06
	40			−19.80
	50			−22.54
Upper layer	30	3.08	0.059	−14.74
	40			−15.32
	50			−15.91

Fig. 7. Cumulative FU release from FU@HZIF-8 at pH 5.5 and 7.4. FU, fluorouracil; FU@HZIF, fluorouracil-loaded zeolitic-imidazolate framework.

the confined structure created by the metal-ligand interactions is opened due to the sensitivity of their coordination bonds in the acidic environment [59,60], hence, releasing more drugs from the interior part of HZIF-8. The gradual dissociation of this HZIF-8 framework causes FU to be desorbed at a constant rate [61].

Therefore, by using HZIF-8, an improved loading capacity of FU can be achieved, and at the same time, FU can be effectively released at a specific pH, which facilitates the targeting of a specific
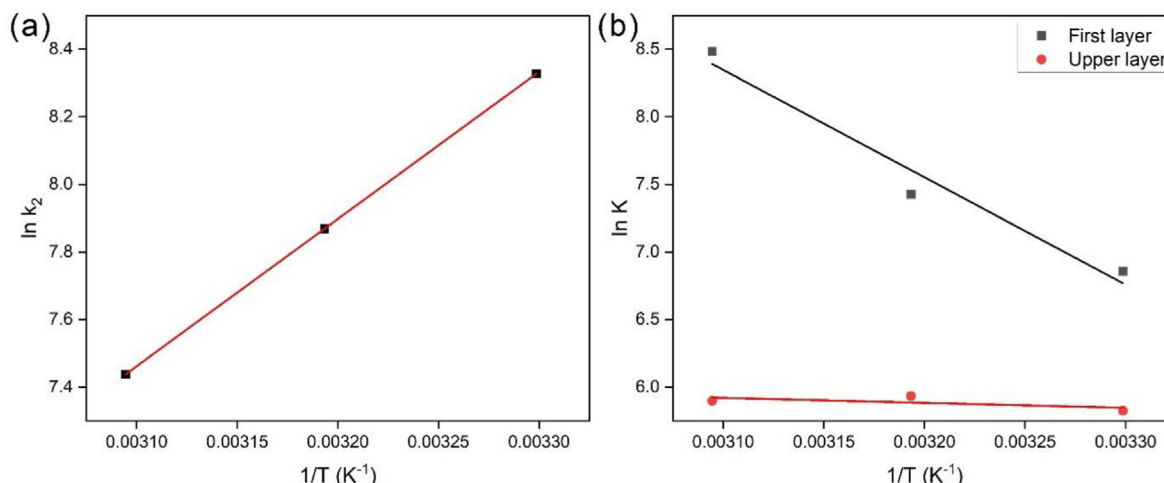

Fig. 6. Thermodynamic studies based on (a) PSO constant and (b) BET isotherm constant. BET, Braunauer–Emmett–Teller; PSO, pseudo-second-order.
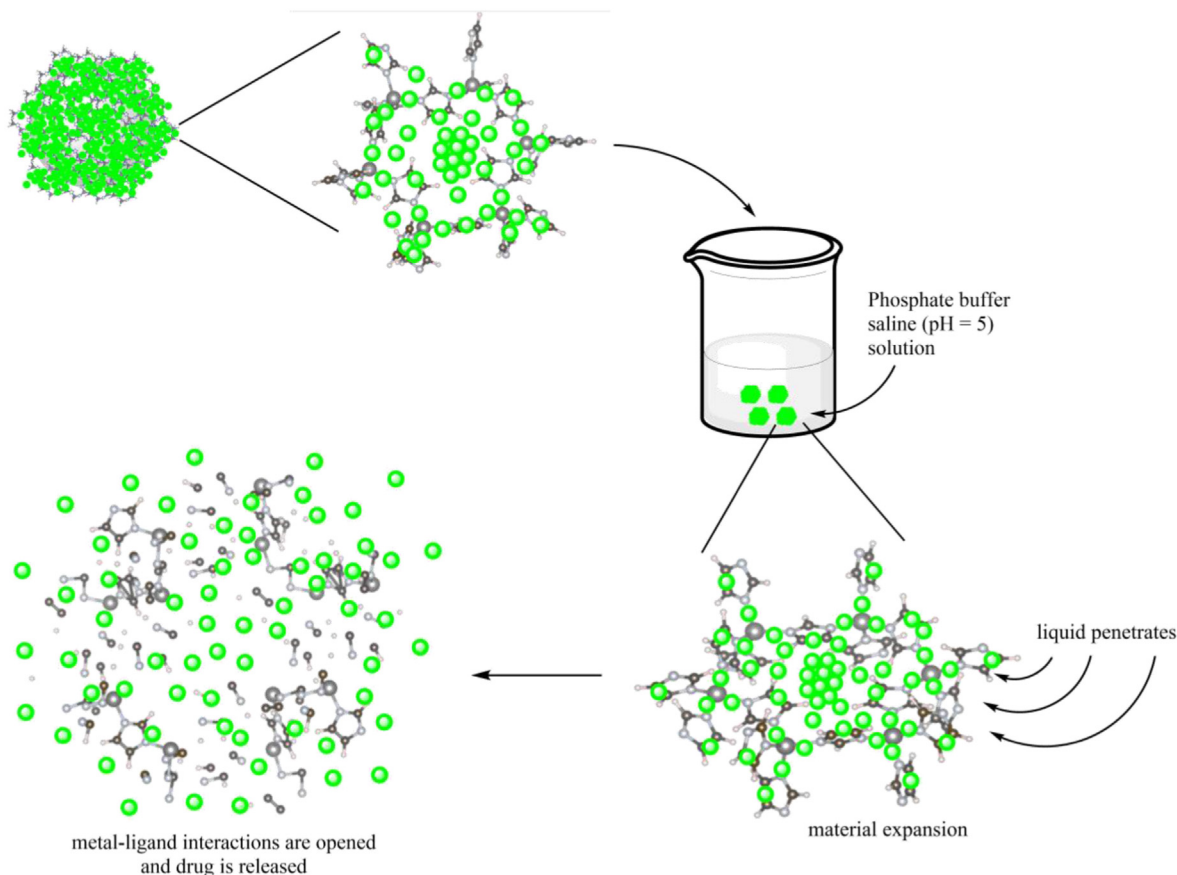
Fig. 8. The schematic mechanism of FU release from FU@HZIF-8. FU, fluorouracil; FU@HZIF, fluorouracil-loaded zeolitic-imidazolate framework.

organ or part of the human body. This stimuli-responsive mechanism may also improve drug control in the circulatory system of the body and prevent drug leakage during delivery to the target. Moreover, this mechanism prevents drug exposure to normal organs or body parts, and thus, potentially reduces the side-effects of the drug, which are more likely to occur in a burst or free drug release. Due to these reasons, the well-controlled therapeutic performance can be employed using HZIF-8 to treat various difficult diseases, such as tumors and cancers [62].

4. Conclusion

In this study, HZIF-8 has been successfully developed as a smart and promising material for the uptake and release system of FU. The rhombic dodecahedron HZIF-8 with the particle size of *ca.* 450 nm possesses a hollow core with a diameter of 180 nm. The shell of HZIF-8 is obtained at *ca.* 135 nm. The surface area and pore volume of HZIF-8 are found at 1727.1 m^2/g and 0.99 cm^3/g, respectively. HZIF-8 gives an excellent performance as a drug carrier for FU; the maximum uptake capacity of FU by HZIF-8 reaches 161.9 mg/g at 40 °C. The adsorption of FU follows the PSO law and multilayer mechanism. According to the isotherm study, the first and upper adsorption layers are, respectively, governed by chemical and physical interaction. The release study exhibits the pH-responsive characteristics of HZIF-8 where a higher and better-controlled release is observed at pH = 5.5 than at pH = 7.4. Therefore, HZIF-8 can be considered a smart and tunable material that can provide flexible and controllable properties to be implemented in various cases of DDS with a specific release mechanism.

Credit author statement

Stefani Agnestasia Anggraini, Conceptualization, methodology, software, visualization, investigation, writing − original draft.

Kevin Adiputra Prasetija, Conceptualization, methodology, software, visualization, investigation, writing − original draft.

Maria Yuliana, Conceptualization, methodology, software, visualization, writing-review and editing, resources, supervision.

Christian Julius Wijaya, Conceptualization, methodology, writing-review and editing, supervision.

Vania Bundjaja, Software, investigation.

Artik Elisa Angkawijaya, Software, investigation.

Yi-Fan Jiang, Software, investigation.

Jindrayani Nyoo Putro, Validation.

Sandy Budi Hartono, Project administration, funding acquisition.

Aning Ayucitra, Project administration, funding acquisition.

Shella Permatasari Santoso, Data curation.

Suryadi Ismadji, Resources, validation.

Felycia Edi Soetaredjo, Resources, data curation.

Data availability

Data will be made available on request.

Acknowledgment

References

[1] E. Shakerzadeh, Efficient carriers for anticancer 5-fluorouracil drug based on the bare and M-encapsulated (M = Na and Ca) B40 fullerenes; in silico investigation, J. Mol. Liq. 343 (2021), 116970, https://doi.org/10.1016/j.molliq.2021.116970.

[2] S. Akay, B. Kayan, A. Jouyban, F. Martínez, Solubility and dissolution thermodynamics of 5-fluorouracil in (ethanol + water) mixtures, J. Mol. Liq. 333 (2021), 116038, https://doi.org/10.1016/j.molliq.2021.116038.

[3] H. Kaur, G.C. Mohanta, V. Gupta, D. Kukkar, S. Tyagi, Synthesis and characterization of ZIF-8 nanoparticles for controlled release of 6-mercaptopurine drug, J. Drug Deliv. Sci. Technol. 41 (2017) 106−112, https://doi.org/10.1016/j.jddst.2017.07.004.

[4] M.X. Wu, Y.W. Yang, Metal-organic framework (MOF)-Based drug/cargo delivery and cancer therapy, Adv. Mater. 29 (2017), https://doi.org/10.1002/adma.201606134.

[5] A.L. Li, F. Ke, L.G. Qiu, X. Jiang, Y.M. Wang, X.Y. Tian, Controllable synthesis of metal-organic framework hollow nanospheres by a versatile step-by-step assembly strategy, CrystEngComm 15 (2013) 3554−3559, https://doi.org/10.1039/c2ce26636.

[6] L. Feng, K.Y. Wang, J. Powell, H.C. Zhou, Controllable synthesis of metal-organic frameworks and their hierarchical assemblies, Matter 1 (2019) 801−824, https://doi.org/10.1016/j.matt.2019.08.022.

[7] Y. Han, F. Wang, J. Zhang, Design and syntheses of hybrid zeolitic imidazolate frameworks, Coord. Chem. Rev. 471 (2022), https://doi.org/10.1016/j.ccr.2022.214759.

[8] D. Zhao, D.J. Timmons, D. Yuan, H.C. Zhou, Tuning the topology and functionality of metal-organic frameworks by ligand design, Acc. Chem. Res. 44 (2011) 123−133, https://doi.org/10.1021/ar100112y.

[9] S.T. Meek, J.A. Greathouse, M.D. Allendorf, Metal-organic frameworks: a rapidly growing class of versatile nanoporous materials, Adv. Mater. 23 (2011) 249−267, https://doi.org/10.1002/adma.201002854.

[10] M. Eddaoudi, H. Li, O.M. Yaghi, Highly porous and stable metal-organic frameworks: structure design and sorption properties, J. Am. Chem. Soc. 122 (2000) 1391−1397, https://doi.org/10.1021/ja9933386.

[11] I. Erucar, S. Keskin, Efficient storage of drug and cosmetic molecules in biocompatible metal organic frameworks: a molecular simulation study, Ind. Eng. Chem. Res. 55 (2016) 1929−1939, https://doi.org/10.1021/acs.iecr.5b04556.

[12] H.J. Lee, W. Cho, M. Oh, Advanced fabrication of metal−organic frameworks: template-directed formation of polystyrene@ZIF-8 core−shell and hollow ZIF-8 microspheres, Chem. Commun. 48 (2012) 221−223, https://doi.org/10.1039/c1cc16213f.

[13] H. Zheng, Y. Zhang, L. Liu, W. Wan, P. Guo, A.M. Nyström, X. Zou, One-pot synthesis of metal-organic frameworks with encapsulated target molecules and their applications for controlled drug delivery, J. Am. Chem. Soc. 138 (2016) 962−968, https://doi.org/10.1021/jacs.5b11720.

[14] D.-N. Liu, C.-J. Wang, Y.-M. Xiao, C. Liu, D. Luo, Z.-X. Zhu, S. Chen, Y.-Y. Wang, Synthesis of ZIF-8-based multifunctional shell and sustained release of drugs, Inorg. Chem. Commun. 114 (2020), 107773, https://doi.org/10.1016/j.inoche.2020.107773.

[15] M. Gomar, S. Yeganegi, Adsorption of 5-fluorouracil, hydroxyurea and mercaptopurine drugs on zeolitic imidazolate frameworks (ZIF-7, ZIF-8 and ZIF-9), Microporous Mesoporous Mater. 252 (2017) 167−172, https://doi.org/10.1016/j.micromeso.2017.06.010.

[16] P. Horcajada, C. Serre, A.C. Mckinlay, R.E. Morris, Biomedical applications of metal-organic frameworks, in: D. Farrusseng (Ed.), Metal-Organic Frameworks: Applications from Catalysis to Gas Storage, first ed., Wiley-VCH Verlag GmbH & Co, Weinheim, Germany, 2011, pp. 215−250.

[17] J. della Rocca, D. Liu, W. Lin, Nanoscale metal-organic frameworks for biomedical imaging and drug delivery, Acc. Chem. Res. 44 (2011) 957−968, https://doi.org/10.1021/ar200028.

[18] H. Huang, J.R. Li, K. Wang, T. Han, M. Tong, L. Li, Y. Xie, Q. Yang, D. Liu, C. Zhong, An in situ self-assembly template strategy for the preparation of hierarchical-pore metal-organic frameworks, Nat. Commun. 6 (2015) 1−8, https://doi.org/10.1038/ncomms9847.

[19] M.A. Simon, E. Anggraeni, F.E. Soetaredjo, S.P. Santoso, W. Irawaty, T.C. Thanh, S.B. Hartono, M. Yuliana, S. Ismadji, Hydrothermal synthesize of HF-free MIL-100(Fe) for isoniazid-drug delivery, Sci. Rep. 9 (2019) 1−11, https://doi.org/10.1038/s41598-019-53436-3.

[20] Y. Devi, I. Ang, F.E. Soetaredjo, S.P. Santoso, W. Irawaty, M. Yuliana, A.E. Angkawijaya, S.B. Hartono, P.L. Tran-Nguyen, S. Ismadji, Y.H. Ju, An iron-carboxylate-based metal−organic framework for Furosemide loading and release, J. Mater. Sci. (2020), https://doi.org/10.1007/s10853-020-05009-3.

[21] R. Abazari, A.R. Mahjoub, F. Ataei, A. Morsali, C.L. Carpenter-Warren, K. Mehdizadeh, A.M.Z. Slawin, Chitosan immobilization on bio-MOF nanostructures: a biocompatible pH-responsive nanocarrier for doxorubicin release on MCF-7 cell lines of human breast cancer, Inorg. Chem. 57 (2018) 13364−13379, https://doi.org/10.1021/acs.inorgchem.8b01955.

[22] K.S. Park, Z. Ni, A.P. Côté, J.Y. Choi, R. Huang, F.J. Uribe-Romo, H.K. Chae, M. O'Keeffe, O.M. Yaghi, Exceptional chemical and thermal stability of zeolitic imidazolate frameworks, Proc. Natl. Acad. Sci. USA 103 (2006) 10186−10191, https://doi.org/10.1073/pnas.0602439103.

[23] M.Y. Li, J. Liu, R. Gao, D.Y. Lin, F. Wang, J. Zhang, Design and synthesis of zeolitic tetrazolate-imidazolate frameworks, Mater Today Adv 10 (2021), https://doi.org/10.1016/j.mtadv.2021.100145.

[24] G. Zhu, L. Cheng, R. Qi, X. Liu, Hollow mesoporous metal-organic framework microdisks via a solid template-based approach and post-synthetic wet-chemical etching for protein loading, ChemNanoMat 6 (2020) 589−597, https://doi.org/10.1002/cnma.202000061.

[25] Y.X. Tan, F. Wang, J. Zhang, Design and synthesis of multifunctional metal-organic zeolites, Chem. Soc. Rev. 47 (2018) 2130−2144, https://doi.org/10.1039/c7cs00782e.

[26] A. Akhundzadeh Tezerjani, R. Halladj, S. Askari, Different view of solvent effect on the synthesis methods of zeolitic imidazolate framework-8 to tuning the crystal structure and properties, RSC Adv. 11 (2021) 19914−19923, https://doi.org/10.1039/D1RA02856A.

[27] J.J. Beh, J.K. Lim, E.P. Ng, B.S. Ooi, Synthesis and size control of zeolitic imidazolate framework-8 (ZIF-8): from the perspective of reaction kinetics and thermodynamics of nucleation, Mater. Chem. Phys. 216 (2018) 393−401, https://doi.org/10.1016/j.matchemphys.2018.06.022.

[28] Y. Zhang, Y. Jia, M. Li, L. Hou, Influence of the 2-methylimidazole/zinc nitrate hexahydrate molar ratio on the synthesis of zeolitic imidazolate framework-8 crystals at room temperature, Sci. Rep. 8 (2018) 9597, https://doi.org/10.1038/s41598-018-28015-7.

[29] E. Binaeian, S. Maleki, N. Motaghedi, M. Arjmandi, Study on the performance of Cd^{2+} sorption using dimethylethylenediamine-modified zinc-based MOF (ZIF-8-mmen): optimization of the process by RSM technique, Separ. Sci. Technol. 55 (2020) 2713−2728, https://doi.org/10.1080/01496395.2019.1655056.

[30] M. Khalfaoui, S. Knani, M.A. Hachicha, A.B. Lamine, New theoretical expressions for the five adsorption type isotherms classified by BET based on statistical physics treatment, J. Colloid Interface Sci. 263 (2003) 350−356, https://doi.org/10.1016/S0021-9797(03)00139-5.

[31] K. Chen, T. Zhang, X. Chen, Y. He, X. Liang, Model construction of micro-pores in shale: a case study of Silurian Longmaxi Formation shale in Dianqianbei area, SW China, Petrol. Explor. Dev. 45 (2018) 412−421, https://doi.org/10.1016/S1876-3804(18)30046-6.

[32] M.K. Antoniou, E.K. Diamanti, A. Enotiadis, A. Policicchio, K. Dimos, F. Ciuchi, E. Maccallini, D. Gournis, R.G. Agostino, Methane storage in zeolite-like carbon materials, Microporous Mesoporous Mater. 188 (2014) 16−22, https://doi.org/10.1016/j.micromeso.2013.12.030.

[33] M.A. Hourieh, M.N. Alaya, A.M. Youssef, F. El-Sejariah, Analysis of nitrogen sorption data of chemically activated carbon by the application of adsorption models based on surface coverage and volume filling of micropores. 1. Phosphoric acid activated carbons, Adsorpt. Sci. Technol. 17 (1999) 675−688, https://doi.org/10.1177/026361749901700806.

[34] T.R. Sahoo, B. Prelot, Adsorption processes for the removal of contaminants from wastewater, in: Nanomaterials for the Detection and Removal of Wastewater Pollutants, Elsevier, 2020, pp. 161−222, https://doi.org/10.1016/B978-0-12-818489-9.00007-4.

[35] U.A. Edet, A.O. Ifelebuegu, Kinetics, isotherms, and thermodynamic modeling of the adsorption of phosphates from model wastewater using recycled brick waste, Processes 8 (2020) 665, https://doi.org/10.3390/pr8060665.

[36] S. Karaca, A. Gürses, M. Ejder, M. Açıkyıldız, Kinetic modeling of liquid-phase adsorption of phosphate on dolomite, J. Colloid Interface Sci. 277 (2004) 257−263, https://doi.org/10.1016/j.jcis.2004.04.042.

[37] A.S. Ghatbandhe, H.G. Jahagirdar, M.K.N. Yenkie, S.D. Deosarkar, Evaluation of thermodynamic parameters of 2, 4-dichlorophenoxyacetic acid (2, 4-D) adsorption, J. Chem. 2013 (2013) 1−6, https://doi.org/10.1155/2013/519304.

[38] G.Y. Abate, A.N. Alene, A.T. Habte, Y.A. Addis, Adsorptive removal of basic green dye from aqueous solution using humic acid modified magnetite nanoparticles: kinetics, equilibrium and thermodynamic studies, J. Polym. Environ. 29 (2021) 967−984, https://doi.org/10.1007/s10924-020-01932-3.

[39] Y.S. Ho, G. McKay, Pseudo-second order model for sorption processes, Process Biochemistry 34 (1999) 451−465, https://doi.org/10.1016/S0032-9592(98)00112-5.

[40] Y.S. Ho, A.E. Ofomaja, Pseudo-second-order model for lead ion sorption from aqueous solutions onto palm kernel fiber, J. Hazard Mater. 129 (2006) 137−142, https://doi.org/10.1016/j.jhazmat.2005.08.020.

[41] J.-P. Simonin, On the comparison of pseudo-first order and pseudo-second order rate laws in the modeling of adsorption kinetics, Chem. Eng. J. 300 (2016) 254−263, https://doi.org/10.1016/j.cej.2016.04.079.

[42] H. Liu, L. Chen, J. Ding, A core-shell magnetic metal organic framework of type Fe3O4@ZIF-8 for the extraction of tetracycline antibiotics from water samples followed by ultra-HPLC-MS analysis, Microchim. Acta 184 (2017) 4091–4098, https://doi.org/10.1007/s00604-017-2442-6.

[43] A.O. Dada, A.P. Olalekan, A.M. Olatunya, Dada, Freundlich Langmuir, Temkin and dubinin-radushkevich isotherms studies of equilibrium sorption of Zn 2+ unto phosphoric acid modified rice husk, IOSR Journal of Applied Chemistry (IOSR-JAC. 3 (2012) 38–45, https://doi.org/10.9790/5736-0313845.

[44] M.A. Al-Ghouti, D.A. Da'ana, Guidelines for the use and interpretation of adsorption isotherm models: a review, J. Hazard Mater. 393 (2020), https://doi.org/10.1016/j.jhazmat.2020.122383.

[45] N. Yuan, H. Cai, T. Liu, Q. Huang, X. Zhang, Adsorptive removal of methylene blue from aqueous solution using coal fly ash-derived mesoporous silica material, Adsorpt. Sci. Technol. 37 (2019) 333–348, https://doi.org/10.1177/0263617419827438.

[46] C.H. Giles, D. Smith, A. Huitson, A general treatment and classification of the solute adsorption isotherm. I. Theoretical, J. Colloid Interface Sci. 47 (1974) 755–765.

[47] S. Liu, Cooperative adsorption on solid surfaces, J. Colloid Interface Sci. 450 (2015) 224–238, https://doi.org/10.1016/j.jcis.2015.03.013.

[48] K. Behere, S. Yoon, n-Layer BET adsorption isotherm modeling for multimeric Protein A ligand and its lifetime determination, J. Chromatogr. B 1162 (2021), 122434, https://doi.org/10.1016/j.jchromb.2020.122434.

[49] T.L. Easun, F. Moreau, Y. Yan, S. Yang, M. Schröder, Structural and dynamic studies of substrate binding in porous metal-organic frameworks, Chem. Soc. Rev. 46 (2017) 239–274, https://doi.org/10.1039/C6CS00603E.

[50] Y. Qin, X. Han, Y. Li, A. Han, W. Liu, H. Xu, J. Liu, Hollow mesoporous metal-organic frameworks with enhanced diffusion for highly efficient catalysis, ACS Catal. 10 (2020) 5973–5978, https://doi.org/10.1021/acscatal.0c01432.

[51] M.C. Tonucci, L.V.A. Gurgel, S.F. de Aquino, Activated carbons from agricultural byproducts (pine tree and coconut shell), coal, and carbon nanotubes as adsorbents for removal of sulfamethoxazole from spiked aqueous solutions: kinetic and thermodynamic studies, Ind. Crop. Prod. 74 (2015) 111–121, https://doi.org/10.1016/j.indcrop.2015.05.003.

[52] S. Chowdhury, R. Mishra, P. Saha, P. Kushwaha, Adsorption thermodynamics, kinetics and isosteric heat of adsorption of malachite green onto chemically modified rice husk, Desalination 265 (2011) 159–168, https://doi.org/10.1016/j.desal.2010.07.047.

[53] S. Chen, C. Qin, T. Wang, F. Chen, X. Li, H. Hou, M. Zhou, Study on the adsorption of dyestuffs with different properties by sludge-rice husk biochar: adsorption capacity, isotherm, kinetic, thermodynamics and mechanism, J. Mol. Liq. 285 (2019) 62–74, https://doi.org/10.1016/j.molliq.2019.04.035.

[54] S. Duan, J. Li, X. Liu, Y. Wang, S. Zeng, D. Shao, T. Hayat, HF-free synthesis of nanoscale metal-organic framework NMIL-100(Fe) as an efficient dye adsorbent, ACS Sustain. Chem. Eng. 4 (2016) 3368–3378, https://doi.org/10.1021/acssuschemeng.6b00434.

[55] Q. Wang, Y. Sun, S. Li, P. Zhang, Q. Yao, Synthesis and modification of ZIF-8 and its application in drug delivery and tumor therapy, RSC Adv. 10 (2020) 37600–37620, https://doi.org/10.1039/D0RA07950B.

[56] H. Maeda, M. Brandon, A. Sano, Design of controlled-release formulation for ivermectin using silicone, Int J Pharm 261 (2003) 9–19, https://doi.org/10.1016/S0378-5173(03)00293-X.

[57] S. Dash, P.N. Murthy, L. Nath, P. Chowdhury, Kinetic modeling on drug release from controlled drug delivery systems, Acta Poloniae Pharmaceutica - Drug Research 67 (2010) 217–223.

[58] C.-Y. Sun, C. Qin, X.-L. Wang, G.-S. Yang, K.-Z. Shao, Y.-Q. Lan, Z.-M. Su, P. Huang, C.-G. Wang, E.-B. Wang, Zeolitic imidazolate framework-8 as efficient pH-sensitive drug delivery vehicle, Dalton Trans. 41 (2012) 6906, https://doi.org/10.1039/c2dt30357d.

[59] W. Cai, J. Wang, C. Chu, W. Chen, C. Wu, G. Liu, Metal-organic framework-based stimuli-responsive systems for drug delivery, Adv. Sci. 6 (2019), https://doi.org/10.1002/advs.201801526.

[60] S. Angelos, N.M. Khashab, Y.W. Yang, A. Trabolsi, H.A. Khatib, J.F. Stoddart, J.I. Zink, pH clock-operated mechanized nanoparticles, J. Am. Chem. Soc. 131 (2009) 12912–12914, https://doi.org/10.1021/ja9010157.

[61] J. Zhuang, C.H. Kuo, L.Y. Chou, D.Y. Liu, E. Weerapana, C.K. Tsung, Optimized metal-organic-framework nanospheres for drug delivery: evaluation of small-molecule encapsulation, ACS Nano 8 (2014) 2812–2819, https://doi.org/10.1021/nn406590.

[62] P. Mi, Stimuli-responsive nanocarriers for drug delivery, tumor imaging, therapy and theranostics, Theranostics 10 (2020) 4557–4588, https://doi.org/10.7150/thno.38069.